41st AIAA/ASME/SAE/ASEE Joint Propulsion Conference & Exhibit
10 - 13 July 2005, Tucson, Arizona

AIAA 2005-3649

# Unsteady Nozzle Design for Pulse Detonation Engines

Zachary C. Owens[*] and Ronald K. Hanson[†]
*Stanford University, Stanford, CA, 94305*

**A quasi-one-dimensional, Euler model with detailed finite-rate chemistry is used to conduct a parametric assessment of area ratio effects on the performance of unsteady nozzles in a pulse detonation engine (PDE). Using results from the parametric study, design criteria are suggested for evaluating optimal contraction and expansion nozzle area ratios. In particular, a method using simple isentropic analysis is revealed for identifying optimal expansion area ratio for a given tube configuration. To validate the parametric analysis, three nozzle sections are tested in the Stanford experimental PDE facility. Time resolved thrust and specific impulse ($I_{sp}$) measurements are made for each nozzle and compared to simulated results. Additionally, Schlieren imaging is used to investigate the blowdown gasdynamics in each of the three nozzles. Comparisons between simulated and measured impulse data are addressed using insights gathered from the flow visualization. Resulting analysis indicates that multi-dimension wave phenomena are important for nozzles with converging sections. Over-prediction of $I_{sp}$ by the model is attributed to an inability to accurately capture the pressure in the plateau region, as well as the inability to accurately model the DDT process. The relative contribution of each of these effects is quantified. Experimental measurements validate trends observed in the parametric study and reveal that an appropriately optimized diverging nozzle produces the largest single-cycle $I_{sp}$ augmentation. The applicability of single-pulse results to realistic multi-cycle engines is discussed, with emphasis on the importance of maintaining high reactant fill pressure between multi-pulse cycles. To this effect, the inclusion of a minimal throat section is addressed as a plausible solution despite its deleterious impact on single-cycle performance.**

## Nomenclature

$A_{exit}/A_{throat}$ = expansion area ratio
$A_{throat}/A_{tube}$ = contraction area ratio
$\mathrm{A_i}$ = species i
$[\mathrm{A_i}]$ = concentration of species i
$CJ$ = Chapman-Jouguet state
$DDT$ = deflagration-to-detonation transition
$E$ = energy per unit volume
$\mathbf{F}$ = convective flux vector
$F_x$ = thrust
$g$ = gravitational acceleration
$h$ = enthalpy per unit mass
$I_{sp}$ = specific impulse
$k_b$ = backward rate coefficient
$k_b$ = forward rate coefficient
$m$ = mass
$nr$ = number of reaction equations
$ns$ = number of species
$p$ = pressure
$P_3$ = plateau pressure
$P_{amb}$ = ambient pressure
$P_{fill}$ = reactant fill pressure

---

[*] Graduate Student, Aeronautics & Astronautics, Building 520, Room 520 I, Stanford, CA, 94305. Student Member
[†] Professor, Mechanical Engineering, Building 520, Room 520 E, Stanford, CA, 94305. Fellow AIAA

$P_{head}$ = head wall pressure
$P_i$ = partial pressure of species i
$P_{o,avg}$ = time averaged $P_{head}$
$P_{spark}$ = spark region pressure
$P_{wall}$ = internal wall pressure
$\boldsymbol{Q}$ = area-variation source term
$R_i$ = specific gas constant for species i
$S$ = flux surface
$t$ = time
$t_{cycle}$ = time from ignition until $P_{wall} = P_{amb}$
$\boldsymbol{U}$ = conserved variable vector
$u$ = axial velocity
$v_i'$ = stoichiometric coefficient of reactant
$v_i''$ = stoichiometric coefficient of product
$\boldsymbol{W}$ = species production rate
$Y_i$ = mass fraction of species i
$\rho$ = mass density

## I. Introduction

Pulse detonation engines are currently an active area of propulsion research due to their potential for increased performance and reduced mechanical complexity in comparison to more conventional chemical propulsion systems[1]. Although idealistic analysis suggests the pulsed propulsion cycle can be thermodynamically more efficient than its steady-flow counterparts[2], it remains to be shown whether a practical device can be developed to exploit these inherent advantages. Critical to the success of the PDE concept is the implementation of a nozzle capable of efficiently converting as much of the thermal energy in the exhaust gases into usable propulsive force. While optimal nozzle design for steady, constant pressure, propulsion systems is well-established and relatively straight-forward, the problem of designing nozzles for pulsed propulsion systems poses a significantly greater challenge due to the transient nature of the flowfield.

Many previous computational and experimental PDE nozzle studies have been conducted and presented in the literature. A detailed literature review of work prior to 2001 was performed by Kailasanath[1], and more recent efforts have been chronicled by Wu[2] and Cooper[3]. Topics of most recent interest include nozzle performance at reduced back pressures,[3,4] multi-cycle nozzle performance,[2,5] and impulse augmentation using ejectors.[6,7] Several key nozzle design issues have arisen as a result of these most recent studies. Computational studies by Morris[4] and experiments conducted by Cooper[3] reveal that appropriately designed nozzles can provide increasing impulse enhancement over the straight tube extension as the ambient pressure is decreased. Both studies consider single-shot operation where reactant fill pressure is held constant with respect to a variable ambient condition. Consequently, multi-cycle PDEs will only be able to achieve these large impulse enhancements provided a method of maintaining a high fill-to-ambient pressure ratio between cycles is identified. Yungster[5] also comments on the importance of maintaining high fill pressures between cycles as high expansion ratio nozzles lead to significant over-expansion losses during purging and refilling. As a means of circumventing overexpansion losses, Allgood et. al.[6,7] have been investigating the use of ejectors, which entrain ambient gas into the exit stream. Wu et al.[2] simulated a multi-cycle, airbreathing PDE and demonstrated the use of a nozzle with a 0.56 contraction ratio as a means of maintaining higher fill pressures. Additionally, they noted that the convergent section had the benefit of decreasing the Mach number of the reactants between cycles, which has the effect of lowering stagnation pressure losses due to energy addition. These losses are proportional to the square of the flow Mach number.

Previous studies were successful in identifying the most determinative criteria governing unsteady nozzle performance. This list of criteria includes expansion area ratio, contraction area ratio, nozzle contour (conical, bell, plug, etc.), partial fill effects, and nozzle pressure ratio. In this paper we choose to focus on the most fundamental geometric criteria on this list, nozzle expansion and contraction ratio. In a steady, constant pressure, propulsion systems, the nozzle throat is chosen to maintain chamber pressure while minimizing stagnation pressure losses. In an unsteady PDE the contraction ratio has the additional role of controlling cycle frequency (blowdown time) and the system of reflecting waves which is established in the combustion chamber.[8] As in the case of the steady system, the expansion ratio should be chosen to optimally expand the combustion products to ambient pressure. However, unlike the steady system the stagnation pressure in the PDE chamber is time variant, and this must be appropriately accounted for when choosing an optimal expansion ratio.

In this work a high-order accuracy, chemically reacting, quasi-one-dimensional Euler code was developed to parametrically assess the role of the contraction and expansion area ratios on PDE performance. From these results guidelines are derived for choosing optimal area ratios for an unsteady PDE. In particular a simple analytic means of predicting optimal expansion area ratio is identified. Considerations for multi-cycle PDEs operating at reduced ambient pressures will also be addressed. Guided by the results of the parametric study, three nozzles were built and tested in the Stanford interchangeable, planar nozzle facility. Time-resolved impulse measurements were made in each nozzle and were spatially resolved on each thrust surface (e.g. head wall, converging section, diverging section). Comparisons of the experiments to computational results are made and discrepancies addressed. To further aid in assessing the ability of the computations to accurately predict unsteady nozzle blowdown phenomena, Schlieren images of the blowdown process in each of the three nozzles are also presented.

## II. Computational Model

The unsteady, compressible, quasi-one-dimensional Euler equations are used as an approximate model of gasdynamics in this study. Real detonation waves exhibit multi-dimensional structures and create complex systems of reflecting waves when propagating through variable area nozzles. Nozzle separation is also an inherently viscous, multi-dimension phenomenon that cannot be simulated with this equation set. Nevertheless, while the model will be inadequate for capturing these multi-dimensional, viscous flow features, it will provide a computationally inexpensive platform from which to conduct parametric nozzle studies. Additionally, quasi-one-dimensional models have been shown in the past to predict PDE flowfield variables in good agreement with experimental data.[8,9,10] The equation set, accounting for finite-rate chemical reactions, can be written as follows:

$$\frac{\partial \overline{U}}{\partial t} + \frac{1}{S}\frac{\partial \overline{FS}}{\partial x} = \overline{Q} + \overline{W} \tag{1}$$

The conserved variable vector, flux vector, area-variation source term and chemical source term are given by:

$$\overline{U} = \begin{bmatrix} \rho \\ \rho u \\ E \\ \rho Y_1 \\ \rho Y_2 \\ \vdots \\ \rho Y_{ns-1} \end{bmatrix}, \overline{F} = \begin{bmatrix} \rho u \\ \rho u^2 + p \\ (E+p)u \\ \rho u Y_1 \\ \rho u Y_2 \\ \vdots \\ \rho u Y_{ns-1} \end{bmatrix}, \overline{Q} = \begin{bmatrix} 0 \\ \frac{p}{S}\frac{\partial S}{\partial x} \\ 0 \\ 0 \\ 0 \\ \vdots \\ 0 \end{bmatrix}, \overline{W} = \begin{bmatrix} 0 \\ 0 \\ 0 \\ \dot{w}_1 \\ \dot{w}_2 \\ \vdots \\ \dot{w}_{ns-1} \end{bmatrix} \tag{2}$$

The fluid is considered to be mixture of thermally perfect gases and the equation of state can be written as shown in Eq. (3). Equation (4) represents the volumetric energy content of the gas mixture.

$$p = \sum_{i=1}^{ns} p_i = \rho\left(\sum_{i=1}^{ns} Y_i R_i\right)T = \rho R T \tag{3}$$

$$E = -p + \rho\left(\frac{u^2}{2} + h\right) \tag{4}$$

The chemical source terms in Eq. (2) are computed with the aid of a chemical mechanism which consists of a set of *nr* elementary chemical reactions of the form:

$$\sum_{i=1}^{ns} \nu'_{i,n} A_i \Leftrightarrow \sum_{i=1}^{ns} \nu''_{i,n} A_i \tag{5}$$

The mass production term for each species $A_k$ can be evaluated by summing the creation and destruction rates in each of the relevant *nr* reactions:

$$\dot{w}_k = M_k \sum_{n=1}^{nr} \left( v''_{k,n} - v'_{k,n} \right) \left[ k_f \prod_{i=1}^{ns} [A_i]^{v'_{i,n}} - k_b \prod_{i=1}^{ns} [A_i]^{v''_{i,n}} \right] \tag{6}$$

In order to obtain maximum versatility, the flow solver utilizes the CHEMKIN[11] gas-phase subroutine library and thermodynamic database. This permits existing chemical mechanisms and species data written in the CHEMKIN format to be easily integrated into the flow solver. In this study we consider stoichiometric $C_2H_4/O_2$ and use a slightly modified version of the 21 species, 33 reaction reduced mechanism developed by Varatharajan.[12] Per the suggestion of Morris[8] the 33 forward reactions described in the original mechanism are made reversible with the reverse reaction rate computed using the equilibrium constant.

Before solving Eq. (1) it is first split using the Strang[13], second-order, time-step-splitting procedure. In this procedure Eq. (1) is recast into two equations; one which describes fluid convection with no chemical reaction as shown in Eq. (7), and the other which describes chemical reaction in a motionless fluid as shown in Eq. (8).

$$\frac{\partial \overline{U}}{\partial t} + \frac{1}{S}\frac{\partial \overline{FS}}{\partial x} = \overline{Q} \tag{7}$$

$$\frac{d\overline{U}}{dt} = \overline{W} \tag{8}$$

Equation (7) is discretized over the computational domain in finite-volume form and convective fluxes at cell interfaces are computed using a 3rd-order, ENO-Roe scheme with an entropy fix. The left and right eigenvectors of the flux Jacobian, required to move into and out of characteristic space in the ENO algorithm, are evaluated using Roe averages at the cell interfaces as described in Ref. (14). The fluid convection equation is advanced in time using a 3rd-order, explicit, TVD Runge-Kutta algorithm.[15] The chemical reaction equation, Eq. (8), is a stiff system of ordinary differential equations. This system is solved using the publicly available LSODE package. In order to couple Eqs. (7) and (8), the solver first advances the chemical reactions by a half time step, followed by a full time step of fluid convection, proceeded by a second half time step of chemical reaction. In operator notation this looks like:

$$\overline{U}^{\,n+1} = L_{chem}^{\Delta t/2} L_{conv}^{\Delta t} L_{chem}^{\Delta t/2} \overline{U}^{\,n} \tag{9}$$

Since the chemical reaction steps are separate from the fluid convection step it is convenient that the gas chemistry can be frozen simply by removing the chemical reaction operators in Eq. (9). In the simulations presented here using the 21 species, 33 reaction mechanism, the fluid convection step requires a small fraction of the computational expense required to update the stiff chemical reaction equations.

# III. Area Ratio Effects on Nozzle Performance

## A. Test Configuration

Using the model described in the previous section, a parametric assessment of the effect of contraction and expansion area ratio on nozzle performance was conducted. Figure (1) depicts the test configuration used in this computational study. In all cases a stoichiometric mixture of $C_2H_4/O_2$ was used to fill the entire tube volume, including the nozzle section. The detonation was initiated directly using a 1 mm long region of high temperature and pressure gasses adjacent to the head wall as the spark region. For all cases the spark temperature was set to 3000 K while the ratio of $P_{spark}/P_{fill}$ was fixed at 30. Using a fixed $P_{spark}$ for all tested values of $P_{fill}$ was avoided since at the lowest fill pressures the high $P_{spark}$ value leads to highly overdriven detonation wave and has a non-negligible effect on the resulting impulse. For all fill pressures tested the model computes average detonation velocity to within 2.5% of Chapman-Jouguet value computed using STANJAN[16], and the pulsating nature of the wave speed is observed as described by Yungster.[17] Chapman-Jouguet flow properties are reproduced nearly exactly at the highest tested fill pressures with maximum deviations on the order 5% at the lowest fill pressures. Detonation formation and propagation are computed at a constant grid resolution of 0.1 mm. This grid resolution is too coarse to resolve

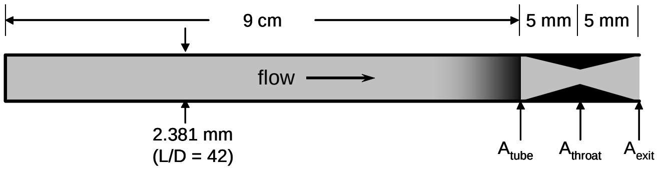

**Figure 1. Configuration used for parametric analysis of area ratio effects. Tube length and nozzle length are fixed while nozzle contraction and expansion area ratios are varied by changing contraction and expansion nozzle angles. Detonation formation and propagation are computed with the fully reactive set of equations until the detonation reaches the nozzle inlet at which point the chemistry is frozen for the remainder of the blowdown.**

the reaction zone, especially at high fill pressures, but shows high fidelity for reproducing the Chapman-Jouguet state as indicated above.

The fully reacting equations are solved using 0.1 mm grid resolution until the detonation front has reached the nozzle entrance, at which point the chemistry is frozen and the remainder of the blowdown is computed at 0.4 mm grid resolution. The computed specific impulse is evaluated based on the fuel and oxidizer mass occupying the thrust chamber up to the start of the nozzle section. Consequently, the fuel oxidizer loading is the same for all nozzles cases evaluated at a given fill pressure. In effect, the stoichiometric mixture of $C_2H_4/O_2$ occupying the nozzle section is isolated from the rest of the thrust chamber by a virtual diaphragm until detonation arrival. Since the chemistry is frozen after detonation arrival, the nozzle mixture does not combust and acts only as a tamper mass. As discussed in Ref. (4) the choice of gas composition for the nozzle tamper mass can have a small effect on the resulting impulse. However, for this study the nozzle fluid composition is invariant between cases and is not expected to affect the resulting trends.

The choice to freeze the chemistry after detonation arrival at the nozzle entrance was done to avoid impractical computational expense. Several runs were made to compare frozen cases to runs made with finite-rate kinetics occurring throughout the blowdown. In general the inclusion of finite-rate kinetics in the blowdown has the effect of maintaining higher chamber temperatures due to its ability to capture exothermic recombination reactions. The extra energy release results in slightly higher chamber pressures which translate to increased $I_{sp}$ values on the order of 5% for the cases tested. The role of chemistry in the nozzle is expected to have the most substantial impact on nozzles with large expansion area ratios where nozzle inlet temperatures will be substantially higher then nozzle exit temperatures. In this study we identify optimal expansion ratios which are relatively low, and thus the choice to freeze the chemistry for the nozzle blowdown portion of the cycle is not expected to have a significant impact on the resulting trends.

The nozzle used in the test configuration is a variable-area-ratio, conical nozzle of fixed length. A fixed nozzle length was employed to prevent partial fill effects from masking area ratio effects. The contraction area ratio is adjusted by varying the convergent inlet angle and the expansion area ratio is controlled similarly by varying the divergent nozzle angle. To minimize the impact of using a quasi-one-dimensional model, the nozzle half angles are kept small with the maximum never exceeding 6 degrees. The tube L/D ratio was selected to replicate the experimental PDE at Stanford. The impact of this choice of L/D will addressed as appropriate in the results that follow.

In this study, in contrast to previous single-cycle studies, the reactant fill pressure is varied in parallel with ambient pressure in order to simulate high altitude flight conditions. In each case the reactant initial condition is set by equating the fill pressure to the ambient pressure while setting the fill temperature to 300 K. A single-cycle is defined as the time between detonation initiation and the time at which the head wall of the PDE decays to ambient pressure. As discussed previously, multi-cycle simulations have revealed the difficulty in maintaining chamber pressures above the ambient value during refilling. Equating the fill pressure and ambient pressure was chosen to more closely approximate current multi-cycle operation. It should be emphasized that PDE performance increases substantially as the fill-to-ambient pressure ratio is increased.[3,4] Although this effect is not considered explicitly in this work, the proposed design criteria that follows are not strongly reliant on the assumption that $P_{fill} = P_{amb}$.

Sixteen nozzles were considered in this study in addition to the straight tube extension which serves as a reference condition. The contraction area ratio for this set of nozzles varied between 0.4 and 1.0, representing maximum throat obstruction and no throat obstruction, respectively. The expansion area ratio was increased incrementally until an optimal point was identified for each contraction area ratio. The range of expansion ratios was not known *a priori*, and consequently the number and exact geometry of each nozzle in the test matrix was not predetermined. This process was repeated at five different fill pressures ranging from 1 atm down to 0.05 atm.

## B. Simulation Results

In Fig. (2) single-cycle $I_{sp}$ is plotted versus nozzle area ratio for the case of 1 atm fill pressure. The left running axis shows nozzles with increasing expansion area ratio while the right running axis shows nozzles with a decreasing level of throat obstruction. The projection of each curve onto each of the 3-axis planes is shown with a dashed line. The projection on the back-left surface illustrates very clearly that single cycle $I_{sp}$ decreases as throat obstruction increases. This effect occurs because the impulse loss incurred on the convergent section is generally larger then the increase in impulse incurred at the head due to wave reflections and increased blowdown time. The vertical separation between curves on this surface reveals the effect of expansion area ratio. The three upper curves are very close to the optimal expansion area ratio, whereas the lower curve, representing $A_e/A_t$=1.25, is under-expanded and has a decreased level of performance.

The parabolic shapes of the curves on the back-right surface reveal the optimal expansion area ratio for each nozzle configuration. While there are not enough data points to refine this optimal value exactly, the approximate optimal expansion ratio is very close to 1.75 for all four contraction ratios illustrated. This reveals that optimal expansion area ratio is not a strong function of the level of throat obstruction. This point will be examined further shortly. Although expansion ratios above 2 are not shown, the downward slope will continue as performance drops due to overexpansion.

Several previous experimental and computational studies have indicated that nozzles do not show increased performance over the straight-tube extension at high back pressures. The reference straight-tube case for the 1 atm condition illustrated in Fig. (2) has an $I_{sp}$ of 180.2 sec. Figure (2) reveals that all optimally expanded nozzles configurations either match or exceed this level of performance. The straight-tube will only show significant performance enhancement over nozzles with expansion ratios that deviate substantially from this optimal point. For instance a purely diverging nozzle with an expansion ratio of 4 (not shown) produces a single cycle Isp of 168 seconds for the conditions of Fig (2). This is 7% lower in performance then the straight-tube case, yet the optimally expanded diverging nozzle depicted in Fig. (2) outperforms the straight-tube case by 4%.

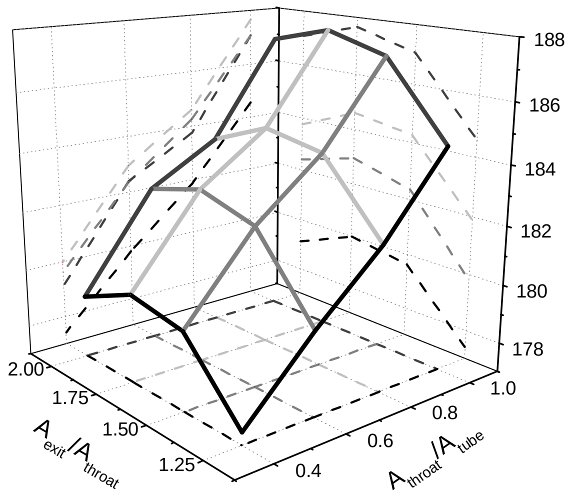

**Figure 2. Single-cycle $I_{sp}$ versus area ratio. Reference $I_{sp}$ for the straight-tube extension is 180.2 sec. ($P_{fill}$ = $P_{amb}$ = 1 atm)**

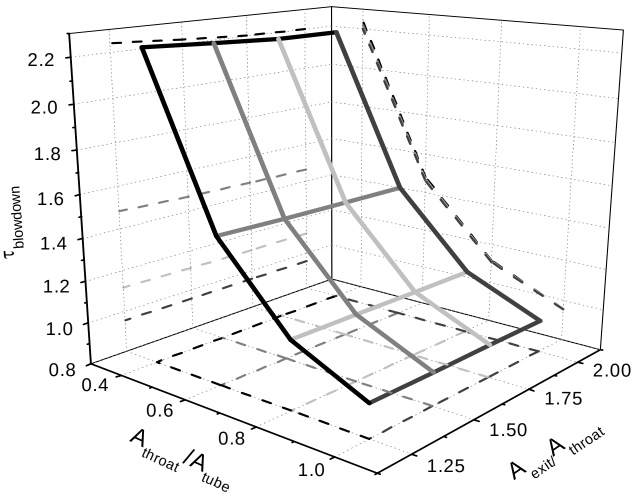

**Figure 3. Normalized single-cycle blowdown time versus area ratio. Blowdown times have been normalized by the straight-tube blowdown time. ($P_{fill}$ = $P_{amb}$ = 1 atm)**

In Fig. (3) the normalized single-cycle blowdown time is plotted as a function of area ratio. The blowdown times for each nozzle configuration have been normalized by the straight-tube blowdown time. The projection on the back right surface of the plot reveals the high sensitivity of blowdown time to contraction area ratio. Nozzles with contraction area ratios of 0.4 take over twice as long to complete a single cycle relative to the straight-tube case. On the other hand, purely diverging nozzles have slightly shorter blowdown times then the straight-tube case. For multi-cycle PDEs, where operating frequency contributes to performance, cycle time is an important consideration. The projection on the back left surface of Fig. (3) reveals that blowdown time is relatively insensitive to expansion ratio.

Figures (2) and (3) portray the optimally-expanded, diverging nozzle as the top performer because it attains the highest $I_{sp}$ with the shortest blowdown time. However, as indicated previously, a multi-cycle PDE will not operate efficiently unless the reactants can be combusted at high pressure and low Mach number. From this standpoint the purely diverging nozzle is the worst choice as its lack of a throat leads to higher velocities and lower chamber pressures at the end of a cycle. Ultimately, designing the contraction ratio for a multi-cycle PDE will be done as an iterative trade-off between the single-cycle performances losses resulting from throat constriction versus the multi-cycle benefit of increasing the combustion efficiency by optimizing the state of the reactants before detonation initiation.

In designing the expansion area ratio for a steady nozzle the optimal point can be found for a given ambient pressure using isentropic analysis provided the stagnation pressure of the combustion chamber is known. A similar procedure can be done for the unsteady PDE provided a suitable definition for the design stagnation pressure is identified. In this work the single-cycle, time-averaged head wall pressure is proposed for this purpose. This pressure is defined as indicated in Eq. (10).

$$P_{o,avg} = \frac{\int_{o}^{tcycle} P_{head} \cdot dt}{t_{cycle}} \tag{10}$$

Using this definition $P_{o,avg}$ has been plotted in Fig. (4) for each of the sixteen different nozzle configurations for the 1 atm condition. Figure (4) indicates that $P_{o,avg}$ decreases as the level of throat obstruction increases. This may go against initial intuition, however, the effect is a result of the prolonged amount of time it takes the plateau head pressure to relax back to the ambient condition for cases of increased throat obstruction. During this relaxation period the average head pressure is lower than the plateau condition ($P_3$), which dominates the early stages of the cycle. Consequently, configurations with the short blowdown times have $P_{o,avg}$ values which are closer to $P_3$ than configurations with long blowdown times. Figure (4) also reveals that the $P_{o,avg}$ is not sensitive to expansion area ratio. This is a convenience to the designer since it decouples the defined design stagnation pressure from the quantity being optimized.

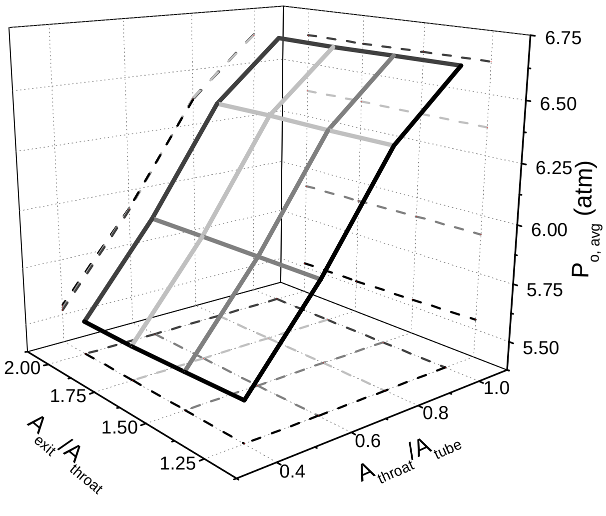

**Figure 4. $P_{o,avg}$ versus area ratio. Reference $P_{o,avg}$ for the straight-tube is 6.53 atm. ($P_{fill}$ = $P_{amb}$ = 1atm)**

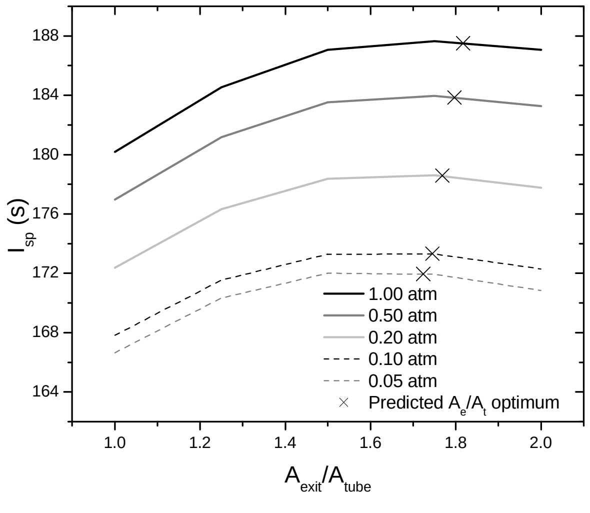

**Figure 5. Diverging nozzle $I_{sp}$ versus expansion area ratio. For each case $P_{fill}$ = $P_{amb}$.**

With regard to Figure (4) a general point can also be made that if the fill pressure is at least equal to the ambient pressure then there will be some performance enhancement obtainable through the implementation of a nozzle. This is the case because the time-averaged stagnation pressure during a single cycle is necessarily higher then the ambient value as a result of detonative compression. This elevated stagnation pressure can always be expanded to some extent to extract additional performance. The level of performance augmentation that results from this expansion is directly proportional to $P_{o,avg}/P_{amb}$. This was indirectly shown in references (3) and (4) where $P_{o,avg}$ was replaced by $P_3$ and $P_{fill}$, respectively. All three of these reference stagnation pressures are directly proportional to one another.

In the course of this study simulation data was generated in order to reproduce Figs. (2) through (4) at four additional fill pressure conditions extending down to 0.05 atm. The trends already discussed with regard to the 1 atm case apply to each of the cases investigated at lower pressures, and for this reason these plots will not be shown. Instead, to summarize the effects of reduced fill pressure, in Fig. (5) we plot $I_{sp}$ versus expansion ratio for a series of purely diverging nozzles operating under different pressure conditions. The first major conclusion to draw from Fig. (5) is that performance is directly proportional to fill pressure. The optimized diverging nozzle at 1 atm fill pressure shows a 9% increase in $I_{sp}$ performance over the optimized nozzle at 0.05 atm. The performance increase is directly attributable to the increased effectiveness of the detonation wave in compressing the reactants. The ratio of Chapman-Jouguet pressure to fill pressure ($P_{cj}/P_{fill}$) for the 1 atm case is 33.3, whereas this same ratio for the 0.05 atm case is 29.7. The discrepancy between these values accounts for the observed $I_{sp}$ performance gap between the two cases. This result again emphasizes the importance of maintaining a high $P_{fill}$ in multi-cycle operation. It should be noted that the magnitude of the performance results in Fig. (5) would be shifted upwards for cases where $P_{fill}/P_{amb}$ is greater than unity, although the trends with regard to $P_{fill}$ will persist.

The second point to draw from Fig. (5) is that the optimal area ratio does not change substantially between the various pressure conditions. Again, due to a lack of detailed resolution of the optimal point for each case, the extent of this effect is not fully quantifiable. However, for a given nozzle configuration, $P_{o,avg}/P_{amb}$ will vary directly with $P_{cj}/P_{amb}$ which is by definition equivalent to $P_{cj}/P_{fill}$. It has already been established that $P_{cj}/P_{fill}$ decreases at low fill pressures. Since higher values of $P_{o,avg}/P_{amb}$ lead to nozzles with higher optimal expansion area ratios, it is expected that the low pressure cases will have optimal expansion area ratios below the high pressure cases. This trend is recovered in Fig. (5). Interestingly, steady rocket designers for years have been attempting to design nozzles which optimally expanded under various pressure ratios corresponding to different flight conditions. It appears that a PDE that can recharge its reactants at ambient pressure would accomplish this goal with a fixed expansion area ratio.

The crossed data points in Fig. (5) represent an isentropic prediction of the optimal area ratio, based on $P_{o,avg}$ for the straight-tube at each fill pressure. The isentropic analysis would be most accurate if instead $P_{o,avg}$ for this set of diverging nozzles was used. However, we have chosen to use the straight-tube $P_{o,avg}$ as the reference condition to illustrate its utility in accurately predicting the result even for the diverging nozzles. Using the straight-tube $P_{o,avg}$ is of particular convenience to designers since Witenberger's analytic impulse model[18] can be used to deduce $P_{o,avg}$ for arbitrary mixtures and tube geometries. As evident, this simple analysis is able to reproduce the optimal expansion ratio in close agreement with the model. The accuracy of the predicted value for the 1 atm pressure condition reveals that using the straight tube $P_{o,avg}$ would have also recovered the optimal expansion ratios for the other converging-diverging nozzles to within the resolution afforded in Fig. (2). Nevertheless, the accuracy of using $P_{o,avg}$ from the straight-tube is expected to decrease for nozzles with increasingly high throat obstruction. This simple analysis can be used to identify a starting point for more involved optimization procedures with full scale computational fluid dynamics.

## IV. Experimental Impulse Measurement & Schlieren Imaging

### A. Test Configuration

In order to validate the trends discussed in the parametric study, three nozzle sections were fabricated for testing on the Stanford PDE. The first nozzle, which will be referred to as Insert 1 is a planar (2-D) converging-diverging nozzle with a contraction ratio of 0.4 and an expansion area ratio of 2.0. The second nozzle, Insert 2, is a planar, diverging nozzle with an expansion area ratio of 2.0. Detailed drawings of both nozzle inserts are shown in Fig. (6). The expansion ratio of 2 was chosen to be in close vicinity to the optimal point identified in the parametric study. The third nozzle section, Insert 3, is simply a square channel straight extension. All nozzles considered in these experiments were planar in order to allow Schlieren imaging of the entire nozzle channel. The flow visualization is intended to aid in assessing the validity of using the proposed computation model and helps justify discrepancies between observed and simulated PDE performance.

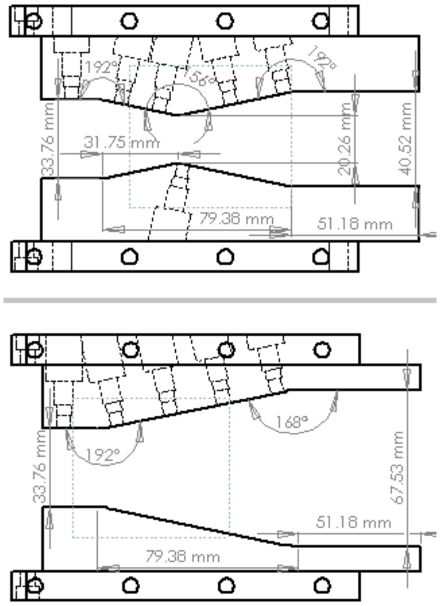

**Figure 6. Nozzle geometry for Insert 1 (top) and Insert 2 (bottom). Nozzle width (into page) is constant and equal to 3.38 cm. The dotted square indicates viewable section during Schlieren imaging.**

*Stanford PDE Facility Description*

The Stanford PDE is 160 cm long with the first 100 cm of tube consisting of 3.81 cm diameter round tube. The L/D ratio is 42 as was the case for the parametric study. The last 60 cm consists of a 20 cm long, constant-area, round-to-square transition, followed by a 20 cm long square recovery section, followed by a 20 cm long, planar nozzle visualization section. The top and bottom surfaces of the nozzle section are removable, allowing arbitrary two-dimensional geometries to be tested.

For this study the facility is operated on a stoichiometric $C_2H_4/O_2$ mixture. The fuel and oxidizer are fed through choked orifices into a jet-in-crossflow mixer where they are premixed just upstream of the head-end injection point. The supply tank pressures of the fuel and oxidizer being fed to this mixer through choked orifices can be independently adjusted in order to change the stoichiometry of the charge. After mixing, the injection plumbing bifurcates and injection occurs at the top and bottom of the tube as illustrated in Fig. (7). The ignition of the premixed gases is initiated when the charge has reached the exit of the tube where the arrival and stoichiometry of the charge can be monitored with a diode laser sensor (not shown).[19,20] It is important to note that these experiments differ slightly from the parametric study since the reactants fully fill the nozzle section as opposed to having a non-reactive tamper mass in the nozzle. After filling is complete, the mixture is ignited with a 100 mJ electric spark which is located 6 cm from the head wall.

The deflagration-to-detonation transition (DDT) is measured using ion probes, and a fully established detonation wave takes approximately 30 cm to develop. At first the detonation wave is slightly overdriven, but the wave speed then decays and remains within 3% of the Chapman-Jouguet value (2.4 km/s for stoichiometric $C_2H_4/O_2$) after passing the measurement station 60 cm from the tube head end. Exhaust gases are discharged from the open end of the PDE into a large, continuously purged dump tank. In this study the tube is operated in single shot-mode only and all experimental results were conducted at $P_{fill}=P_{amb}=1$ atm.

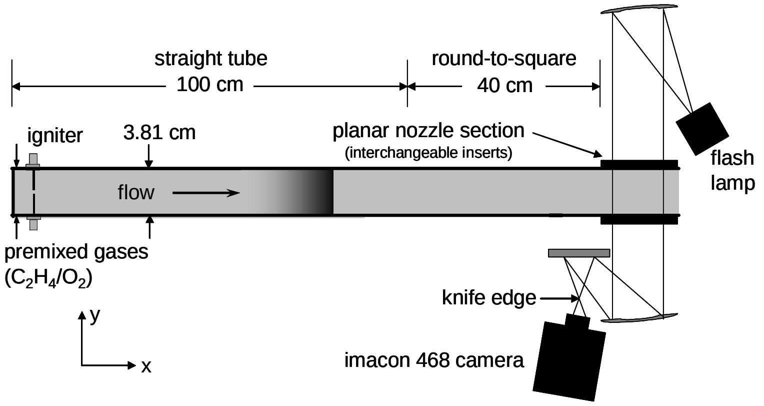

**Figure 7. Stanford PDE with planar, nozzle viewing chamber. Also shown is mirror-based, Z-arrangement Schlieren imaging system.**

*Impulse Measurement Setup*

Time-resolved thrust measurements are made using wall-mounted pressure transducers in each nozzle, as shown in Fig. (6), as well as a transducer in the head wall. All pressure transducers are Kistler model 603B1 and each is connected to its own Kistler model 5010B charge amplifier.

Neglecting viscous effects, the vector force acting on the engine during a single cycle can be determined by integrating the gauge wall pressure over the internal surface of the PDE as in Eq. (11):

$$\vec{F}(t) = \oiint_S P_{wall}(x,t)\,\bar{\bar{I}} \bullet \vec{n}dS \tag{11}$$

It is assumed that wall pressure forces on the top and bottom nozzle surfaces are symmetric, and that the pressure measured at the center of the head wall acts uniformly over this surface. These assumptions reduce $P_{wall}$ to being a function of x (the longitudinal coordinate) and time. In these experiments we are concerned with the x-component of the force vector, which is designated as the thrust, and consequently only measurements at the head wall and nozzle surfaces are required.

Single-cycle impulse is computed by integrating the thrust over the cycle time as in Eq. (12). The cycle time is defined, as before, to be the elapsed time from ignition until the head wall pressure has decayed to the ambient value. The single-cycle specific impulse is computed using Eq. (13).

$$I_{pulse} = \int_0^{t\,cycle} F_x(t)dt \tag{12}$$

$$I_{sp} = \frac{I_{pulse}}{m_{fuel+oxidizer} \cdot g} \tag{13}$$

When reducing the nozzle pressure data from inserts 1 and 2, rather then performing a coarse spatial integration using only the transducer locations as discrete elements, we have fit the pressure data using Hermite interpolating polynomials. The fit is believed to increase the accuracy of the spatial integration within the nozzle and is performed separately on insert data at each time level. The Hermite polynomials were chosen because they produce no overshoot between data points and were observed to maintain the expected curvature in the pressure profile during the nozzle blowdown.

### *Schlieren Imaging Setup*

Figure (7) also shows the mirror-based, Z-arrangement Schlieren system used for this study. The light source is a Hadland Photonics pulsed xenon flash lamp. The system has programmable pulse widths of 20, 50 and 200 μs with corresponding output energies of 125, 375 and 700 J, respectively. Nominally the 50 μs pulse width was used for this study. The Imacon 468 camera system, also manufactured by Hadland Photonics, consists of eight separately intensified CCD arrays (576x385), which are illuminated independently by an internal beam splitter which directs light onto each of the eight channels. The interframe timing and exposure of each channel can be independently adjusted from 10 ns to 1 ms. Internal camera timing events are controlled by a 100 MHz quartz crystal and output triggers are available to program external devices such as the pulsed xenon light source.

Two 14 cm diameter, 61 cm focal length, parabolic mirrors were used to collimate light from the source and refocus the light on the camera side to the location of the knife edge. To consolidate the size of the setup a flat mirror was used in-between the parabolic mirror and the knife edge. Unless otherwise noted, the knife-edge was oriented vertically to provide sensitivity to density gradients along nozzle x-axis.

The dotted square inside each insert in Fig. (6) indicates the viewable section of the nozzle. The windows for the nozzle section were made from 2.8 inch square, 0.5 inch thick sapphire. The hardness of the windows made them extremely resistant to scratching and proved to be a far superior choice over the polycarbonate windows which were used in preliminary experiments. In practice the windows needed to be cleaned after every 10 cycles as the large turbulent boundary layer present at the end of the cycle would leave deposits near the edges of the channel.

## B. Thrust Measurement Results

Thrust measurements for all nozzle inserts will be presented along with the results computed using the quasi-one-dimensional model. The simulated results in this case are computed using full finite-rate chemistry throughout the blowdown. The detonation wave is initiated using a 3000 K, 10 atm, 1.6 cm long spark region centered at the igniter location. In order to save computational expense each case is computed at 1/16 scale and the results are correspondingly rescaled in time by the same factor. This scaling procedure is predicated on the fact the model does not contain any diffusive terms, such as viscosity and thermal conduction, which would be sensitive to an absolute length scale.

Rather then discuss $I_{sp}$ results in conjunction with the thrust measurements, this topic will be deferred until after the Schlieren images for each nozzle insert have been discussed. The imaging results reveal several aspects of the flowfield which lend additional insight into the comparisons of $I_{sp}$ between all nozzle cases. In this section the focus will be on trends in the thrust curves for each nozzle and how they differ from the simulated result.

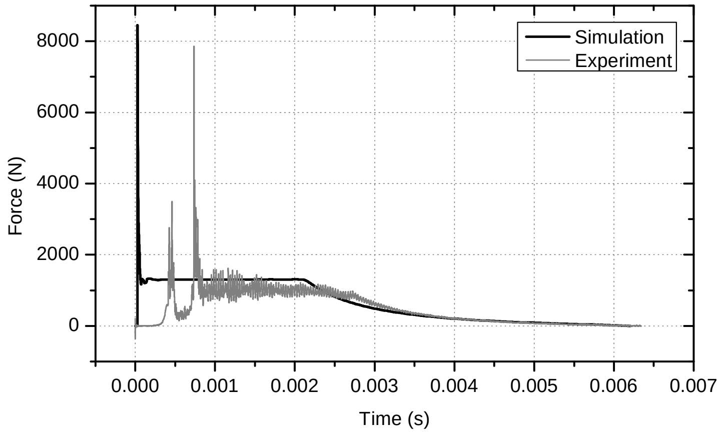

**Figure 8. Straight-tube thrust comparison of simulation versus experiment. Time zero corresponds to ignition and the blowdown is terminated when $P_{head}$ = 1 atm.**

*Straight Tube (Insert 3)*

Insert 3 results are presented first since it represents the baseline case and will have several features in common with the other two nozzle inserts. The first thing to observe in Fig. (8) is the difference between the simulation and the experiment at time-zero. At early times we see that the simulation shows an instantaneous spike corresponding to direct initiation and then reflection of the detonation wave off the head wall. Recall that the igniter is actually offset from the head wall by 6 cm. In the experiment we observe an approximately 0.3 ms delay before the head pressure begins to rise. The spark energy of our ignition system is not sufficient to generate direct initiation, thus the first experimental spike is the result of the left-running DDT process occurring between the spark location and the head wall. The second larger spike in the experimental plot results from a strong reflected shock wave that forms when the right-running detonation wave has become established. This left-running shock wave is generated behind the right-running detonation front due to the large pressure differential between the Chapman-Jouguet state and the relatively low pressure wake occupying the DDT region.

Several attempts of limited success were made at crudely simulating this phenomenon by depositing less energy into the spark region, thereby delaying the coupling of the reaction zone with the lead shock. While it was possible to capture the basic wave behavior of the process described above, the timings of the events were not in good agreement with experiment. The inability of the simulation to capture this early time phenomena is attributed to the lack of diffusion in the purely convective model. In order to model the DDT process, flame speed will have to be calculated accurately which necessitates the inclusion of diffusive terms in the model.

The second important discrepancy between the experiment and the model is with regard to the plateau force. For reasons already discussed, the plateau force will be longer in the simulation as a result of direct initiation. The effect this has on differences between computed and measured $I_{sp}$ will be considered shortly. The magnitudes of the plateau regions are different as well. The plateau force observed in experiments is 24% lower then the computed result. In the past this discrepancy has been attributed to heat transfer effects, which are not accounted for in the model.[21] Another explanation includes accounting for the consequences of turbulence immediately following the reaction zone of a detonation wave, which were shown by White[22] to lead to lower pressure and density then the values predicted by Chapman-Jouguet theory. The conclusive origins of this discrepancy are still unresolved.

*Converging-Diverging Nozzle (Insert 1)*

In Fig. (9), as expected, the effects of direct initiation versus a finite DDT distance are again visible. Note that the spike in the experimental data at time zero is cause by electromagnetic interference from the igniter and does not represent a pressure spike. The discrepancy in plateau force between experiment and simulation is also identical to that described for the straight tube case. These effects will extend to Insert 3 as well and will not be discussed further.

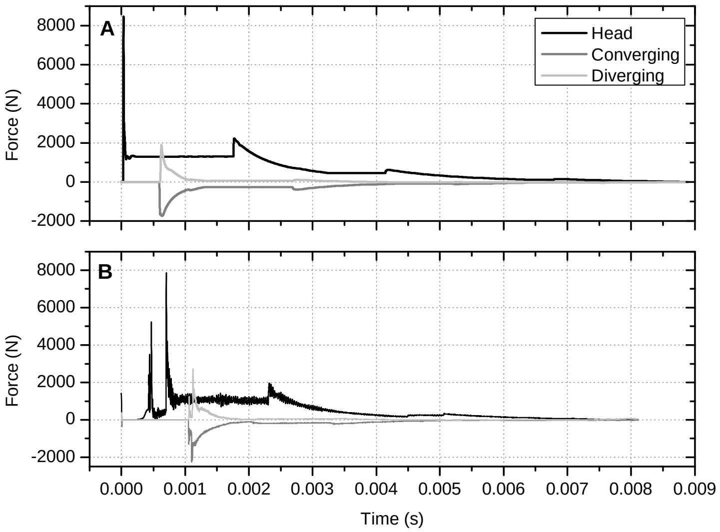

**Figure 9. Converging-diverging nozzle (Insert 1) component thrust comparison of simulation (A) versus experiment (B). Time zero corresponds to ignition and the blowdown is terminated when $P_{head}$ = 1 atm.**

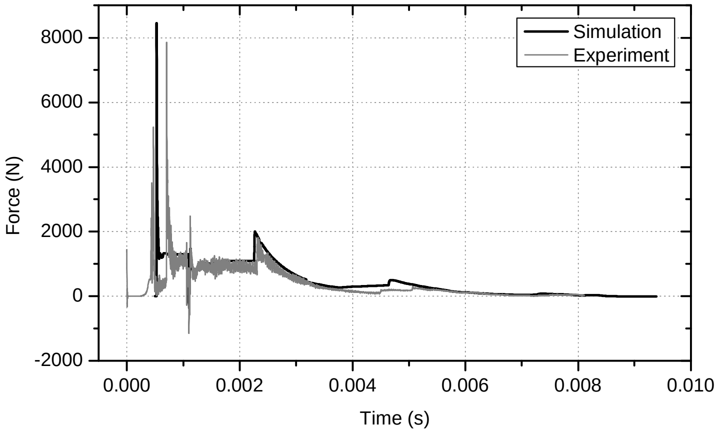

**Figure 10. Converging-diverging nozzle (Insert 1) total thrust comparison of simulation versus experiment. The arrival of the detonation wave at the nozzle has been used to align the features in each plot. Time zero corresponds to ignition in the experimental data only.**

For the C-D nozzle considered here we see that the thrust augmentation provided by the diverging section is nearly identically cancelled by the thrust reduction caused by the converging section during early times after the detonation wave has passed through the nozzle. However, while the diverging section quickly decays to nearly zero thrust, the converging section continues to negatively impact the total impulse throughout much of the cycle. Close examination of Fig. (9) reveals that the diverging thrust only goes negative very near the end of the cycle, indicating that the selected expansion area ratio is very near the optimal point. This helps validate the ability of the quasi-one-dimensional model to identify optimal nozzle geometry.

In Fig. (10) the total thrust for Insert 1 is plotted as a function of time. In this plot the simulated data has been shifted forward so that detonation arrival at the nozzle (indicated by the spike near 1 ms) coincides with the experimental data. In general the model reproduces the experimental trends well; however, the magnitude of all features is higher than observed in experiments. Interestingly, even after the arrival times of the detonation waves at the nozzle section have been aligned, we see that the arrival of the reflected shock from the convergent section at the head wall arrives slightly sooner in the simulation then it does in experiments. This discrepancy of wave arrival time is attributed to a higher acoustic speed in the wake of the detonation for the simulation as compared to the experiment. This phenomenon is discussed in Ref. (8) which attributes the reduced mean acoustic speed in the wake region to heat loss effects not accounted for in the model. This same explanation accounts for the early arrival of the second smaller wave reflection occurring at 5 ms as evident in Fig. (10).

### *Diverging Nozzle (Insert 2)*

In Fig. (11) the thrust components for the strictly diverging nozzle (Insert 2) are plotted as a function of time. We see a significant contribution to impulse from the diverging section in this plot. As was the case for Insert 2, careful examination of Fig. (11) reveals that the force on the diverging section only becomes slightly negative at the end of the cycle. This again indicates that the expansion area ratio is very near the optimal point. The fact that Insert 1 and Insert 2 experiments both show an expansion area ratio of 2 to be near the optimal point confirms the result of the parametric study that optimal expansion ratio is not strongly sensitive to the level of throat obstruction.

In Fig. (12) the total thrust for Insert 2 is plotted versus time. As before the arrival of the detonation wave at the nozzle section for the simulated case has been aligned with the experimentally observed arrival time. Again we see the ability of the model to reproduce the correct trends in thrust, however at a magnitude higher than that observed in the experiment. For the case of the diverging nozzle, which has a very short blowdown time, the total impulse is heavily weighted towards the contribution from the plateau region. Consequently, the ability to predict impulse performance for a diverging nozzle is going to be largely dependent on predicting the plateau conditions at the head end with high accuracy.

## C. Schlieren Imaging Results

To aid in the comparison of simulated to experimental data, Schlieren imaging was performed on all three nozzle inserts. During a single experimental run the light source was programmed for 50 μs pulse width, and during this time up to 8 separate exposures could be taken. In order to image the entire blowdown process many runs were necessary and to ensure repeatability, the first frame of a given time sequence was overlapped with the last frame of the previous sequence. For Inserts 1 and 2 the camera was triggered using the first pressure transducer in the nozzle section. Using this procedure resulted in excellent repeatability since the duration of the DDT process is the least repeatable event, and this took place before the camera was triggered. More care needed to be taken with the straight-tube section since a transducer port was not available close to the nozzle. In this section we will focus the discussion on blowdown gasdynamics and defer its relevance to $I_{sp}$ prediction until the final section.

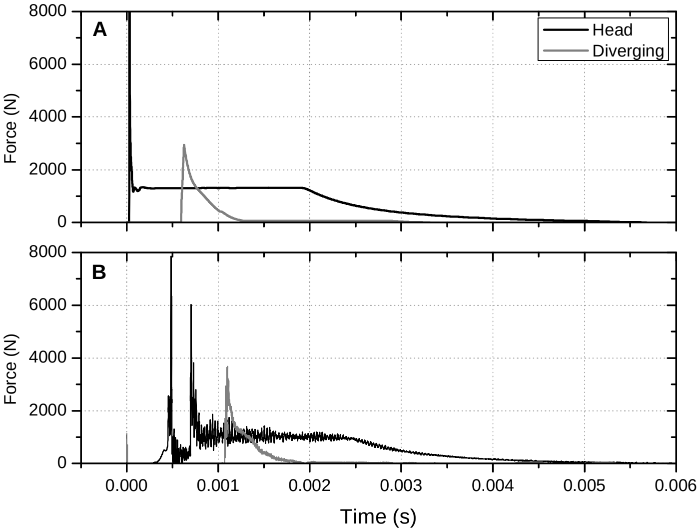

**Figure 11. Diverging nozzle (Insert 2) component thrust comparison of simulation (A) versus experiment (B). Time zero corresponds to ignition and the blowdown is terminated when $P_{head}$ = 1 atm.**

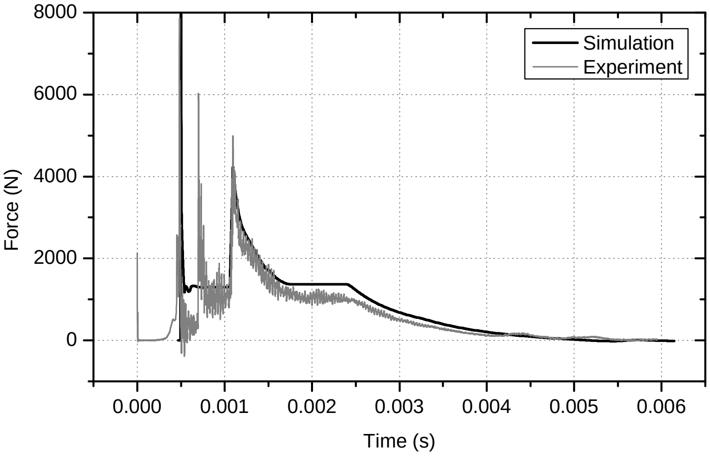

**Figure 12. Diverging nozzle (Insert 2) total thrust comparison of simulation versus experiment. The arrival of the detonation wave at the nozzle has been used to align the features in each plot. Time zero corresponds to ignition in the experimental data only.**

*Straight-Tube (Insert 3)*

In Fig. (13) an 18 frame Schlieren imaging sequence is shown beginning with the arrival of the detonation wave in the nozzle section and concluding with fully turbulent channel flow at the end of the cycle. From 1.07 – 1.08 ms we see the detonation front entering and traversing to the center of the viewable section. Behind the detonation front we see a series of intersecting oblique shock waves which are stationary relative to the detonation front. The existence of this oblique pattern has been observed previously by Edwards et al.[23] and their origin still remains uncertain. An especially intriguing result arising due to the existence of this wave pattern is that flow in this region must be supersonic relative to the detonation front. According to Chapman-Jouguet theory this would require the detonation wave to exist on the weak branch of the Rankine-Hugoniot curve which is forbidden by conventional entropy arguments. However, the turbulent structure hypothesis of White[22], which was referenced previously as an explanation for the decreased pressure in the plateau region, also predicts the existence of supersonic flow behind the detonation front. In his paper[22], White shows that the addition of turbulent terms to the conservation equations precludes the existence of an exact Chapman-Jouguet state as defined by the point of tangency between the Rankine-Hugoniot and the Rayleigh line. Once the tangency condition is removed the arguments that support the inexistence of weak detonations become invalid. White's postulation is neither confirmed nor denied in this study, although presented experimental findings are in support of his theory.

Using White's hypothesis, Edwards et al.[23] suggest the oblique shock pattern is formed because of a large pressure gradient across the boundary layer in the reaction zone behind the detonation front. The pressure gradient is established because the reaction rate in the boundary layer is slower than that of the core flow, thus maintaining the boundary layer closer to the von Neumann pressure, while the core flow has reacted sufficiently to approach the Chapman-Jouguet state. Provided the flow is supersonic relative to the detonation front, this pressure differential would cause sufficient perturbation to generate the oblique shock pattern observed in Fig. (13).

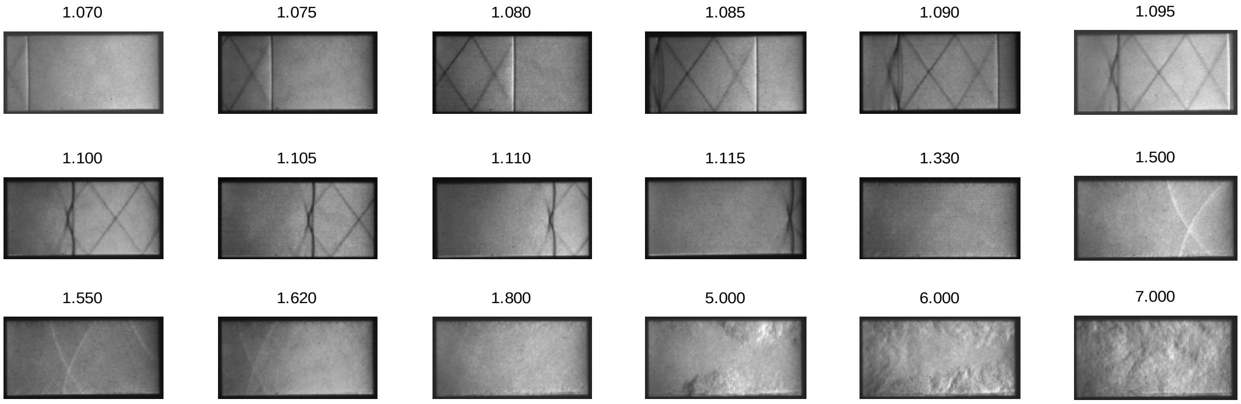

**Figure 13. Straight-tube (Insert 3) blowdown imaging sequence. Numbers above each frame indicate time in milliseconds from ignition. Knife edge is oriented vertically with rightwards positive density gradients appearing lighter.**

Whatever the cause of the oblique shock pattern, it is clear that the strong reflecting shock which comes into view at 1.085 ms is preventing the pattern from reflecting further upstream. This strong reflected normal shock was described previously and is generated by the large pressure differential established between the flow behind the right-running detonation front and the low pressure in the DDT wake region. This wave is traveling extremely fast, as it began as a left-running wave before it reflected off the head wall and proceeded to nearly catch up to the detonation wave by the time it reached the nozzle section.

After the detonation wave and reflected normal shock have exited the tube a brief period of shock-free flow is established until at 1.5 ms a set of left-running oblique shock waves begin moving upstream. Due to the orientation of the knife edge left-moving shocks will appear lighter and right-moving shocks will appear darker. These structures reside in the nozzle section until they move out of the left edge at 1.62 ms. The blowdown continues until at 5 ms turbulent boundary layer separation begins to occur along the top and bottom surfaces of the channel. By 7 ms seconds the channel flow has become fully turbulent. Simulation results suggest that reverse flow, or suction of exhaust gasses back into the tube, does not occur unit several milliseconds after the last frame shown.

### *Converging-Diverging Nozzle (Insert 1)*

In Fig. (14) the passage of the detonation wave through Insert 1 with the knife edge oriented horizontally is shown. The viewable portion of Insert 1 was indicated in Fig. (6). The knife edge has been rotated to this orientation to resolve the system of transverse reflections occurring due to the interaction of the detonation wave with the converging section. The knife edge is positioned in such a fashion that upward-running shocks will appear lighter while downward-running shocks will appear darker.

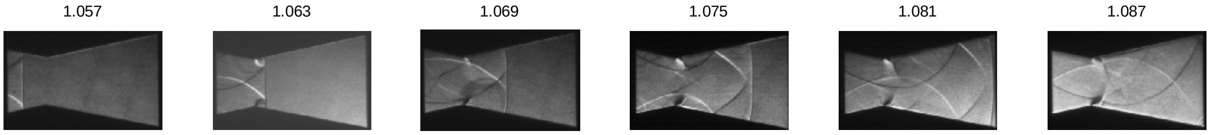

**Figure 14. Converging-diverging nozzle (Insert 1) detonation passage sequence. Numbers above each frame indicate time in milliseconds from ignition. Knife edge is oriented horizontally with upwards positive density gradients appearing darker.**

We see in Fig. (14) that the passage of the detonation through the converging section generates two strong opposing shock waves which intersect each other and proceed to reflect transversely back-and-forth across the nozzle section. Note that these transverse waves prevent the occurrence of the oblique shock pattern observed in the straight-tube. Due to the curvature of these waves and the presence of the diverging section, the upstream part of the same reflected wave will complete its second reflection before the downstream part. This leads to the inflection point visible near the center of the 1.075 ms frame. Strong expansion fans emanating from the throat section indicate the presence of choked flow in the nozzle immediately after detonation passage. The asymmetry of the shading of these expansion fans across the nozzle section is due to the horizontal knife edge orientation. Careful examination of the 1.063 and 1.069 ms frames reveals the propagation of small acoustic disturbances from the location of the pressure transducer ports.

The first six frames of Fig. (15) were taken at identical times to those in Fig. (14) with only difference being the orientation of the knife edge, which is vertical for the later figure. The vertical knife edge orientation reveals several new slip lines and also makes the reflected normal shock visible. These features due not appear in Fig. (14).

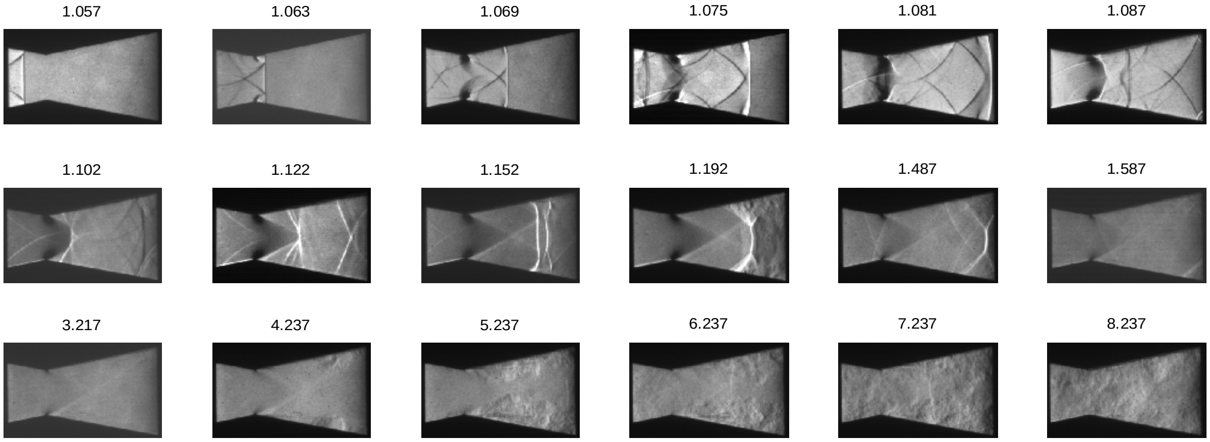

**Figure 15. Converging-diverging nozzle (Insert 1) blowdown imaging sequence. Numbers above each frame indicate time in milliseconds from ignition. Knife edge is oriented vertically with rightwards positive density gradients appearing lighter.**

After the reflected shock exits the nozzle the unsteady starting process begins. The 1.122 ms frame reveals a system of oblique shock waves coalescing into a normal shock at the intersection of the lead mach waves emanating from the expansion fan. Just downstream of this feature two additional oblique shock waves form at the walls of the diverging channel. The upstream feature develops into a normal shock which is pushed downstream and merges with the second shock system, forming a single strong normal shock near the exit of the nozzle as shown in the 1.192 ms frame. Strong, turbulent flow separation is evident behind this shock structure. After 1.487 ms the normal shock weakens and is pushed out of the nozzle at 1.587 ms. Shock-free flow is present in the nozzle until at 4.237 ms turbulent flow separation begins to occur near the nozzle exit. At 5.237 ms a normal shock wave is just visible in the turbulent region at the exit of the nozzle. As part of the nozzle unstarting process the normal shock is sucked upstream and through throat at which point the nozzle unchokes and becomes fully turbulent at 8.237 ms.

*Diverging Nozzle (Insert 2)*

In Fig. (16) the blowdown sequence for the diverging nozzle is shown. The oblique shock pattern is again present in this case until it is quenched by the arrival of the reflecting normal shock at 1.075 ms. Expansion waves are evident at the start of the diverging section immediately after the passage of the detonation wave (1.065 ms) indicating choked flow. After the reflected shock exits the tube at 1.093 ms the nozzle starting process begins. At 1.137 ms two oblique shock waves form just downstream of the expansion fan. Similar to Insert 2, at 1.207 ms the aforementioned oblique shock waves have coalesced into a normal shock which is pushed downstream and merges with the second shock structure present at the exit to form a single strong normal shock. Again, the presence of turbulent, separated flow behind the normal shock is evident. Interestingly, at 1.437 ms the strong normal shock has again bifurcated into two weaker oblique shock structures which proceed to merge a second time into a normal shock (1.687 ms) before being pushed out the nozzle at 1.807 ms. Shock-free flow persists in the nozzle until at 4.597 ms two oblique waves form at exit of the nozzle inducing turbulent separated flow. The unstarting process progresses with the normal shock being sucked into the throat at 5.077 ms after which the flow proceeds to become fully turbulent in the nozzle section.

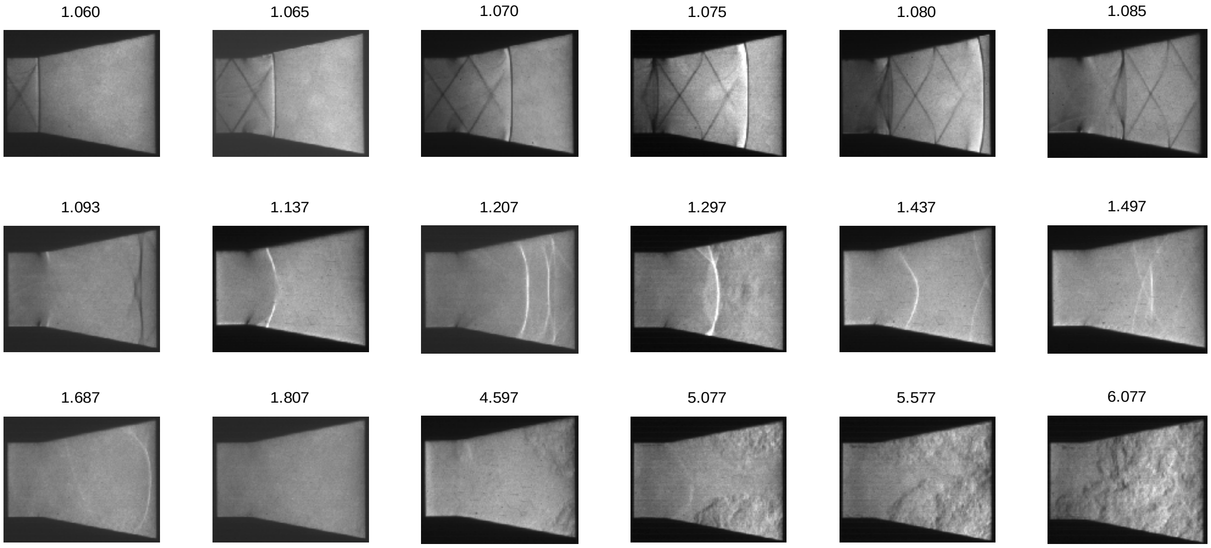

**Figure 16. Diverging nozzle (Insert 2) blowdown imaging sequence. Numbers above each frame indicate time in milliseconds from ignition. Knife edge is oriented vertically with rightwards positive density gradients appearing lighter.**

## D. Specific Impulse Results

The discussion of simulated versus measured specific impulse with regard to each of the three nozzle configurations has been deferred until now so that the results can be considered in light of the flow visualization results. Uncertainty estimates given for the measured values of $I_{sp}$ are computed based on the standard deviation between all values in the data set used to construct the mean values presented in Table 1.

It is of interest to compare the magnitude of the results given for the straight-tube in Table 1 to those offered in previous studies. The computed straight-tube $I_{sp}$ of 178 s agrees exactly with the results presented by Morris in Ref. (10). The experimental result for the straight-tube differs substantially from that presented by Cooper.[24] This discrepancy is a result of the definition of $t_{cycle}$. In ballistic pendulum based impulse measurements made by Cooper, no explicit definition of $t_{cycle}$ is required and a resulting $I_{sp}$ of 170 s is recorded for the stoichiometric, $C_2H_2/O_2$, straight-tube. For reasons of practical applicability in multi-pulse PDEs, where operating frequency is to remain high, we define the end of a cycle as the time when $P_{head}$ has decayed to $P_{amb}$. If the integration of total impulse is extended to long-times, then a value of 165 +/- 7 s is determined. This result is in agreement with the measurement in Ref. (24). The additional impulse at the end of $t_{cycle}$ is the result of a small reflecting wave which persists in the PDE chamber even at long times due to the self-aspirating nature of the PDE blowdown process.[25] This wave results in a small head wall compression above the ambient pressure after each reflection.

| Insert | $I_{sp}$ Head | $I_{sp}$ Converging | $I_{sp}$ Diverging | $I_{sp}$ | $t_{cycle}$ (s) |
|---|---|---|---|---|---|
| 1 - CD | 166.9 | -41.0 | 15.4 | 141.3 +/- 5 | 8.2 |
| 1 - CD | 226.3 | -62.4 | 13.1 | 177.0 | 8.9 |
| 2 - Diverging | 130.9 | 0 | 28.3 | 158.0 +/- 5 | 6.0 |
| 2 - Diverging | 163.2 | 0 | 26.0 | 189.3 | 5.7 |
| 3 - Straight | 139.5 | 0 | 0 | 139.5 +/- 5 | 6.3 |
| 3 - Straight | 178.3 | 0 | 0 | 178.3 | 6.2 |

**Table 1. Comparison of measured and computed single-cycle $I_{sp}$ for each nozzle insert. Rows shaded in gray contain experimental measurements and non-shaded rows contain simulated results. Simulations are performed with direct initiation while experiments have a finite DDT distance. The total impulse used to evaluate each $I_{sp}$ is evaluated over a single $t_{cycle}$.**

As evident from Table 1, the simulated impulse in all cases is above that observed in the experiment. Insert 1 $I_{sp}$ is over predicted by 25%, Insert 2 by 20 % and Insert 3 by 28%. These discrepancies are the result two effects. The first effect is that the simulations undergo direct initiation while the experiments do not. In order to quantify the effect of direct initiation on $I_{sp,}$ the additional plateau region, occurring in the simulated results with respect to the experiment, was subtracted and the $I_{sp}$ was recomputed. The result revealed that in each case 7-9% of the cited discrepancy can be attributed to direct initiation. The remaining disagreement can be attributed to the inability of the model to correctly capture the plateau pressure. As discussed previously, this could either be a heat transfer effect, a result of the White's turbulent structure hypothesis,[22] or a combination of both effects.

Table 1 reveals a large deviation between measured and computed values of head and converging section $I_{sp}$ for Insert 1. The fact that the model deviates from the experiment to the same extent as Inserts 2 and 3 is fortuitous since the over-prediction at the head wall is offset by the over-prediction at the convergent section. This deviation is likely due to the inaccuracy of the quasi-one-dimensional model in predicting a wave reflection event which is truly two-dimensional. As evident in Figs. (14) and (15) a large fraction of the energy from the detonation wave reflection off of the convergent section goes into the system of transverse reflecting waves bouncing back-and-forth across the nozzle channel. The reflection of these waves off the nozzle surface produces only a small thrust component in the axial direction. This would account for why the observed convergent $I_{sp}$ is much lower in absolute magnitude than the simulated value. This same effect also controls the strength of the reflected wave which travels back towards the head wall. The quasi-one-dimensional model is predicting much too strong of a reflected wave since much of this energy is in reality lost in the formation of the transverse shock waves.

The diverging section $I_{sp}$ is well-predicted for Inserts 1 and 2 since the impulse here is not strongly dependent on accurate resolution of any axial shock reflections. The fact that experimental value is actually slightly higher then the simulated value in the diverging section suggests that the transverse reflected waves which go unresolved in the quasi-one-dimensional model actually have an appreciable effect on the impulse. For the case of the diverging nozzle this is in reference to the oblique shock pattern which trails the detonation front.

The results in Table 1 also confirm several results presented in the parametric study. For a single cycle the measured $I_{sp}$ for the diverging nozzle in unequivocally higher then for the converging-diverging nozzle and the straight-tube. This confirms that a diverging nozzle with a nearly optimal expansion area ratio can be designed to outperform the straight-tube case even at high back pressure. Additionally, we see that the nearly optimally expanded converging-diverging nozzle at least matches, if not exceeds the impulse generated by the straight-tube.

The single cycle blowdown time predicted by the quasi-one-dimensional model is within 10% of the experimental value for all three nozzle inserts. This indicates that the turbulent structure and viscous nozzle separation phenomena occurring near the end of the blowdown do not need to be resolved to make an accurate prediction of blowdown time.

## V. Conclusions

A quasi-one-dimensional, Euler model, with detailed finite-rate kinetics was used to study the effects of area ratio on unsteady nozzle performance in a PDE. The results indicate that the contraction area ratio, which largely controls the duration of a single cycle as well as the average pressure and Mach number of the gases at the end of the cycle, will ultimately need to be designed using a detailed multi-cycle analysis model. In general, due to the necessity to maintain high reactant fill pressures and the superior single-cycle performance of diverging nozzles, it is expected that the optimal contraction area ratio will have the minimum throat obstruction required to achieve the desired reactant state between cycles. Alternative refilling schemes will be an important area of future investigation since the magnitude of the performance enhancement provided by nozzles is critically dependent on achieving a high value of $P_{fill}/P_{amb}$.

Results from the parametric study indicate that the optimal expansion area ratio can be identified accurately by performing an isentropic analysis based on the time averaged head wall stagnation pressure for a given PDE geometry. This stagnation pressure is most strongly a function of the contraction area ratio, however, it was shown that the $P_{o,avg}$ value from the straight-tube provides a valid reference point for designing expansion area ratios even for nozzle geometries that deviate substantially from the straight tube. The value of $P_{o,avg}$ for an arbitrary straight-tube geometry and mixture can be deduced from the analytical model presented in Ref. (18).

Time-resolved impulse measurements were made at each thrust surface and compared to simulation results. The largest deviations between simulated and experimental results are due to the inability of the model to capture the DDT event and the inability of models to predict the plateau state behind detonation front. Proposed model idealizations accounting for these inadequacies are discussed.

The nozzle performance trends highlighted in the simulation results are consistent with findings in the experimental data. We observe that appropriately optimized nozzles can be designed to outperform the straight-tube geometry even at high back pressures. In accordance with the parametric study, experimental data reveals that an optimized diverging nozzle produces the highest single-cycle $I_{sp}$.

Schlieren imaging of the blowdown event was performed in three separate nozzle geometries. The results of the imaging in comparison to impulse data reveal that while the quasi-one-dimensional model adequately captures the essential gasdynamics in straight-tubes and diverging nozzles, it is less adept at capturing the magnitude of shock wave reflections occurring in nozzles with a convergent section. This deficiency results from the inability of the model to resolve the two-dimensional nature of the wave structure visible in the Schlieren images. Fortuitously, the over-prediction of the negative impulse on the convergent section is nearly canceled by a corresponding over-prediction in the impulse at the thrust wall due to the shock wave reflection.

## VI. Acknowledgements

The authors would like to thank The Office of Naval Research and Dr. Gabriel Roy (technical monitor) for supporting this research. Additional acknowledgement should be given to Ethan Barbour, Dan Mattison, Ben Gauthier, Dr. Chris Morris and Dr. Matei Radulescu for valuable discussions regarding the content of this work.

## References

[1] Kailasanath, K., "Recent Developments in the Research on Pulse Detonation Engines," *AIAA Journal*, Vol. 41, No. 2, 2003, pp. 145-159.

[2] Wu, Y., Ma, F., and Yang., V., "System Performance and Thermodynamic Cycle Analysis of Airbreathing Pulse Detonation Engines," *Journal of Propulsion and Power*, Vol. 19, No. 4, 2003, pp. 556-567.

[3] Cooper, M. and Shepard, J.E., "The Effect of Transient Nozzle Flow on Detonation Tube Impulse," *40th AIAA Joint Propulsion Conference and Exhibit*, 2004.

[4] Morris, C.I., "Numerical Modeling of Pulse Detonation Engine Gasdynamics and Performance," *42nd AIAA Aerosciences Meeting*, AIAA 2004-0463.

[5] Yungster, S., "Analysis of Nozzle Effects on Pulse Detonation Engine Performance," *41st AIAA Aerosciences Meeting*, AIAA 2003-1316.

[6] Allgood, D., Gutmark, E., and Viswanath, K., "Effects of Exit Geometry on the Performance of a Pulse Detonation Engine," *40th AIAA Aerosciences Meeting*, A02-14342

[7] Allgood, D., Gutmark, E., Rasheed, A., Dean, A.J., "Experimental Investigation of a Pulse Detonation Engine with a Two-Dimensional Ejector," *AIAA Journal*, Vol. 43, No. 2, 2005, pp. 390-398.

[8] Owens, Z., Mattison, D., Barbour, E. Morris, C., and Hanson R., "Flowfield characterization and simulation validation of multiple-geometry PDEs using cesium-based velocimetry," *Proceeding of the Combustion Institute 30*, 2005, pp. 2791-2798.

[9] Mattison, D., Oehlschlaeger, M., Morris, C., Owens, Z., Barbour, E., Jeffries, J. and Hanson, R., "Evaluation of pulse detonation engine modeling using laser-based temperature and OH concentration measurements," *Proceedings of the Combustion Institute 30*, 2005, pp. 2879-2807.

[10] Barbour, E., Owens, Z., Morris, C. and Hanson, R., "The Impact of a Converging-Diverging Nozzle on PDE Performance and its Associated Flowfield," *42nd AIAA Aerosciences Meeting*, AIAA 2004-867.

[11] Kee, R.J, Rupley, F.M., and Miller, J.A., “Chemkin-II: A FORTRAN Chemical Kinetics Package for the Analysis of Gas-Phase Chemical Kinetics,” Tech. Rep. SAND89-8009, Sandia National Laboratories, 1989.

[12] Varatharajan, B., and Williams, F.A., “Ethylene Ignition and Detonation Chemistry, Part 2: Ignition Histories and Reduced Mechanisms,” *Journal of Propulsion and Power*, Vol. 18, No. 2, 2002, pp. 352-362.

[13] Strang, G., “On the Construction and Comparison of Difference Schemes,” *SIAM Journal of Numerical Analysis*, Vol. 5, 1968, pp. 506-517.

[14] Patrick, J., “On the Numerical Solution of the Compressible Navier-Stokes Equations for Reacting and Non-Reacting Gas Mixtures,” Ph.D. Dissertation, Swiss Federal Institute of Technology, Zurich, Diss ETH No. 12030, 1997.

[15] Fedkiw, R.P., “A survey of chemically reacting compressible flows,” Ph.D. Dissertation, Dept. of Mathematics, UCLA, Los Angeles, CA, 1997.

[16] Reynold, W.C., “The Element Potential Method for Chemical Equilibrium Analysis: Implementation in the Interactive Program STANJAN, Version 3,” Tech. rep., Dept. of Mechanical Engineering, Stanford University, Stanford, CA, 1986.

[17] Yungster, S. and Radhakrishnan, K., “Pulsating one-dimensional detonations in hydrogen-air mixtures,” *Combustion Theory and Modeling*, Vol. 8, 2004, pp. 745-770.

[18] Witenberger, E., Austin, J., Cooper, M., Jackson, S., and Shepard, J.E., “An Analytical Model for the Impulse of a Single-Cycle Pulse Detonation Engine,” *Journal of Propulsion and Power*, Vol. 19, No. 1, 2003, pp.22-38.

[19] Barbour, E., Ma, L., Jeffries, J., Hanson, R., Brophy, C., Sinibaldi, J., “Real-Time Measurements of $C_2H_4$ Concentration with Application to PDEs Operating on Oxygen and Air,” *41st Joint Propulsion Conference and Exhibit*, AIAA-2005-4376.

[20] Ma, L., Sanders, S., Jeffries, J., and Hanson, R., “Monitoring and Control of a Pulse Detonation Engine Using a Diode-Laser Fuel Concentration and Temperature Sensor,” *Proceedings of Combustion Institute 29*, 2002, pp. 161-166.

[21] Radulescu, M.I., and Hanson, R.K. “Effect of Heat Loss on Pulse-Detonation-Engine Flow Fields and Performance,” Vol. 21, No. 2., pp. 274-285.

[22] White, D.R., Physics of Fluids, “Turbulent Structure of Gaseous Detonation,” *Physics of Fluids*, Vol. 4, No. 4., 1961, pp. 465-480,

[23] Edwards, D.H., Jones, T.G., Price, B., “Observations of oblique shock waves in gaseous detonations,” Journal of Fluid Mechanics, Vol. 17, Part 1,1963, pp. 21-34

[24] Cooper, M., Jackson, S., Austin, J., Witenberger, E., and Shepard, J.E., “Direct Experimental Impulse Measurements for Detonations and Deflagrations,” *37th AIAA Joint Propulsion Conference and Exhibit*, AIAA 2001-3812.

[25] Bussing, T. and Pappas, G., “An Introduction to Pulse Detonation Engines,” *32nd AIAA Aerosciences Meeting*, AIAA 1994-0263.